ADVANCED FUNCTIONAL MATERIALS

Supporting Information

for *Adv. Funct. Mater.,* DOI: 10.1002/adfm.202204219

Lightweight, Thermally Insulating, Fire-Proof Graphite-Cellulose Foam

Chaoji Chen, Yubing Zhou, Weiqi Xie, Taotao Meng, Xinpeng Zhao, Zhenqian Pang, Qiongyu Chen, Dapeng Liu, Ruiliu Wang, Vina Yang, Huilong Zhang, Hua Xie, Ulrich H. Leiste, William L. Fourney, Shuaiming He, Zhiyong Cai, Zhenqiang Ma, Teng Li, and Liangbing Hu**

Supplementary Information

For

Lightweight, Thermally Insulating, Fire-Proof Graphite-Cellulose Foam

Chaoji Chen[1, a], Yubing Zhou[1, a], Weiqi Xie[2, a], Taotao Meng[1, a], Xinpeng Zhao[1], Zhenqian Pang[2], Qiongyu Chen[2], Dapeng Liu[1], Ruiliu Wang[1], Vina Yang[3], Huilong Zhang[4], Hua Xie[1], Ulrich H. Leiste[5], William L. Fourney[2,5], Shuaiming He[1], Jack Ma[4], Zhiyong Cai[3], Teng Li[2, *], Liangbing Hu[1, *]

[1]Department of Materials Science and Engineering, University of Maryland, College Park, Maryland, 20742.

[2]Department of Mechanical Engineering, University of Maryland, College Park, Maryland, 20742.

[3]Forest Products Laboratory, USDA Forest Service, Madison, Wisconsin, 53726.

[4]Department of Electrical and Computer Engineering, University of Wisconsin – Madison, Madison, Wisconsin, 53706.

[5]Department of Aerospace Engineering, University of Maryland, College Park, Maryland, 20742.

[*] Email: binghu@umd.edu, lit@umd.edu

[a] These authors contributed equally to this work.

Mechanical impact absorbing

A drop tower was used in order to test different materials during impact and evaluate their energy absorbing performance. The drop tower consists of a solid frame which accommodates a guiding rod for the drop weight, a top plate which gets directly impacted by the drop weight, a bottom plate, below the bottom plate a styrofoam cushion, and below that a rigid tower bottom plate (Fig. 3a). All tests were performed, using an identical test procedure. A 6.724 kg drop weight was dropped from a height of 30 cm for impacting the top plate of the dimensions (D x H) 150 mm x 70 mm.

The aluminum plate has a mass of 2.31 kg. Below the top plate, the specimen of interest was placed and centered between the top plate and the bottom plate. The specimens were of the dimension (L x W x H) of 50 mm x 50 mm x 10 mm. The specimens used are made out of aluminum (as reference to calculate the energy dissipation in the whole system), PS foam, CNF-foam, G-CNF-foam, and Cu-G-CNF-foam. Each type of specimen was tested twice. The bottom plate is made out of steel and has the mass of 15.03 kg. The Styrofoam plate between the bottom plate and the ridged tower body plate is used as an impedance mismatch for sensors utilized and performs as a security device in case of overloading the plates.

Once the drop weight is released, a high-speed camera is triggered, recording the impact sequence. The drop weight hits the top plate and the forces are transmitted into the specimen. Depending on the performance of the specimen, the forces are further transmitted into the bottom plate.

Five groups of specimens, namely, aluminum (as reference to calculate the energy dissipation in the whole system), PS foam, CNF-foam, G-CNF-foam, and Cu-G-CNF-foam, were tested using the configuration shown in Fig. S6, of which the velocity of each component was derived from the slope of the linear time-displacement relation recorded by the high speed camera. In each test, the drop weight was crashing towards the plates with an initial velocity V_1 given by gravity. After the crash, all the four components started to go upward with velocity of V_2, V_{top}, and V_{bottom}, respectively. According to energy conservation law, the kinetic energy absorbed by the specimen during the crash can be written as:

$$\Delta E_{kinetic} = \frac{1}{2} M_{weight}(V_1^2 - V_2^2) - \frac{1}{2}(M_{top}V_{top}^2 + M_{bottom}V_{bottom}^2)$$

where M_{weight}, M_{top} and M_{bottom} are the mass of drop weight, top plate and bottom plate, respectively. The calculated test results can be found in Table S1.

As observed from test video, the aluminum bulk was assumed to be rigid and undeformable during the test, it cannot absorb kinetic energy. Therefore, we take this part of energy loss as the energy dissipation in the whole system. Then the real energy absorbed by tested specimen can be written in the form of:

$$\Delta E_{absorbed} = \Delta E_{kinetic} - \Delta E_{dissipation}$$

The averaged energy absorbed by four kinds of foams are listed in Fig. 3c. The G-CNF foam show higher shock absorption energy than pure CNF foam and PS foam. Further ionic crosslinking leads to a higher shock absorption energy of ~10 J. These results suggest that the hybridization of large-sized graphite flakes and the ionic crosslinking both contribute to the improvement of mechanical shock absorption of the graphite-CNF composite foam.

Atomistic modeling

The full atomistic simulations use the ReaxFF potential[1] in the Large-scale Atomic/Molecular Massively Parallel Simulator (LAMMPS) simulation package[2]. ReaxFF potential can be widely used to describe chemical bonds and weak interaction, such as hydrogen bonds and van der Walls force[3]. There are 20 cellulose chains and six graphene flakes in our simulations. Each of cellulose chain contains 22 anhydroglucose units and the size of graphite flake is set as $16\ \text{Å} \times 22\ \text{Å}$. The graphite stack model is shown in Fig. 2f. Considering the influence of thickness of graphite flakes to the formation of foam, flakes constructed by 3 layers and 5 layers of graphene are used to investigate the interaction among different components (Fig. S4). The edges of graphite stack are terminated with randomly-distributed hydrogen or hydroxyl groups. The G-CNF foam is built

according to an approximate mass ratio as graphite: cellulose = 1:1. Initially a very large periodical simulation box was created, which could host spatially-separated 20 CNF chains and six graphite flakes. The entire system was then equilibrated at NPT ensemble at 300 K and 1 atm pressure, using the Nosé−Hoover thermostat and barostat. The timestep is set as 0.5 fs and the periodic boundary conditions are applied in both x-, y- and z-directions for all the models. The arrangement of graphite flakes and cellulose chains in such a large box is responding to the stirring in the experimental synthesis process. The foaming process will be implemented in the equilibration process, in which the periodical simulation box shrinks and form the G-CNF foam. The similar process is arranged in the formation of G foam. All the calculations are relaxed using the conjugate gradient (CG) algorithm to minimize the total energy of the system until the total atomic forces are converged to less than 10^{-9} eV/Å.

Fungi degradation measurement

Fungi preparation: Two wood decay fungi, Postia placenta (Fr.) M.Lars and Lomb. (MAD 698) and Phanerochaete chrysosporium (ME 461) were obtained from the Forest Products laboratory, Madison, Wisconsin and were grown on 2% malt agar, at 27 ^{o}C and 80% relative humidity (RH) for 3-4 weeks prior to place the test samples on the agar plates. Three mold fungi, Aspergillus niger 2.242 provided by University of Virginia, Penicillin chrysogenum PH02 and Trichoderma atraviride ATCC 20476 were grown on 2% malt agar (Difco, Detroit, Mi. USA) for 2-3 weeks. Spore suspensions were prepared by washing the surface of each malt agar plate with 10-15 mL of sterile deionized water (DI) according to ASTM Standard D4445-91.[4] Each mold spore suspension was diluted with DI water to yield 3X107 spores/mL and all three mold suspensions were transferred to a spray bottle. The bottle was adjusted to deliver 1mL inoculum per spray on the test

samples. All Petri dishes containing test samples inoculated with mold spores and decay fungi were incubated at 27 ºC and 80% RH for 12 weeks with interval of every 4 weeks for photograph taking as growth records.

Degradation weight loss measurement: Following the guidelines of AWPA Standard E10-12,[5] test samples were conditioned, weighed and placed on the malt agar plates containing a confluent growth of decay fungi and inoculated with mold spores. On the 12th week, fungal mycelia and mold coverage were brushed from the specimens. Specimens were air dried, reconditioned at 27° C and 80% RH and weighted. Percentage mass loss was calculated for each specimen and reported as an average for each specimen group. **Calculation of porosity based on density:**

$$\emptyset\ (\%) = 1 - \frac{\mathrm{Vt}}{\mathrm{Vv}} * 100\%$$

where $\emptyset$ represents porosity, Vt is the theoretical volume of the foam, and Vv is the bulk volume of Cu-G-CNF foam, including the solid and void components.

Vt (theoretical volume) calculation process: Firstly, we weigh the mass of the Cu-G-CNF foam material and calculate its actual volume (Vv). Secondly, we calculate the mass of cellulose and graphite in the composite foam material by the proportions of cellulose and graphite components. Finally, the theoretical volume of the target material (Vt) is obtained according to the theoretical density of cellulose (1.6 g/cm^3) and graphite (2.26 g/cm^3). We have calculated the porosity of the Cu-G-CNF foam to be ~ 97%.

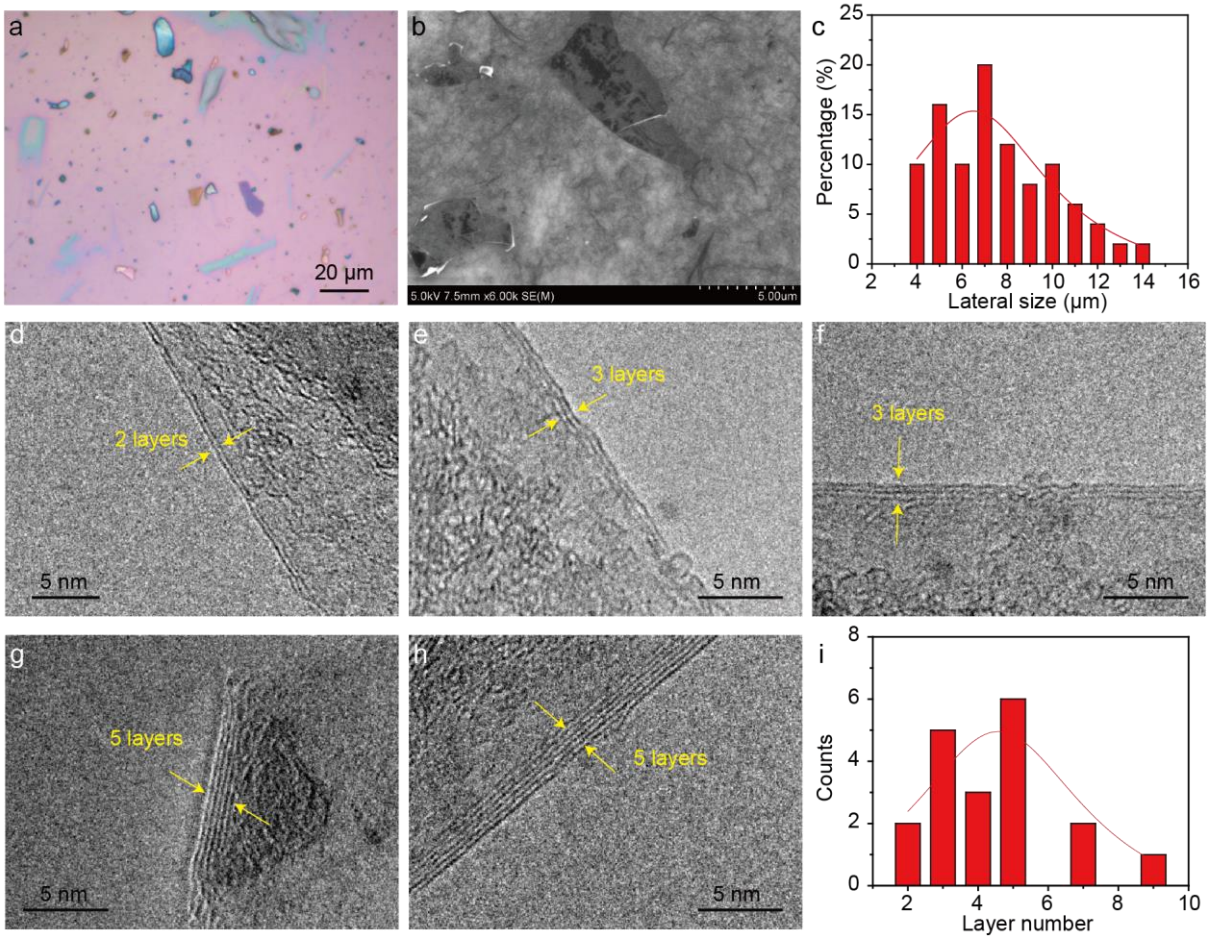

Figure S1. (**a**) Typical optical image and (**b**) SEM image of a diluted graphite-CNF slurry dropped on a SiO_2/Si substrate after drying. The lateral size of individual graphite flakes was determined by the long side. **c**, Lateral size distribution histogram for graphite flakes obtained from a substrate area of ~500 μm × 500 μm. **d-h**, High resolution TEM images of the folded edges of the graphite flakes. The layered structures with periodical fringes indicate the layer number. (i) Layer number distribution histogram for graphite flakes.

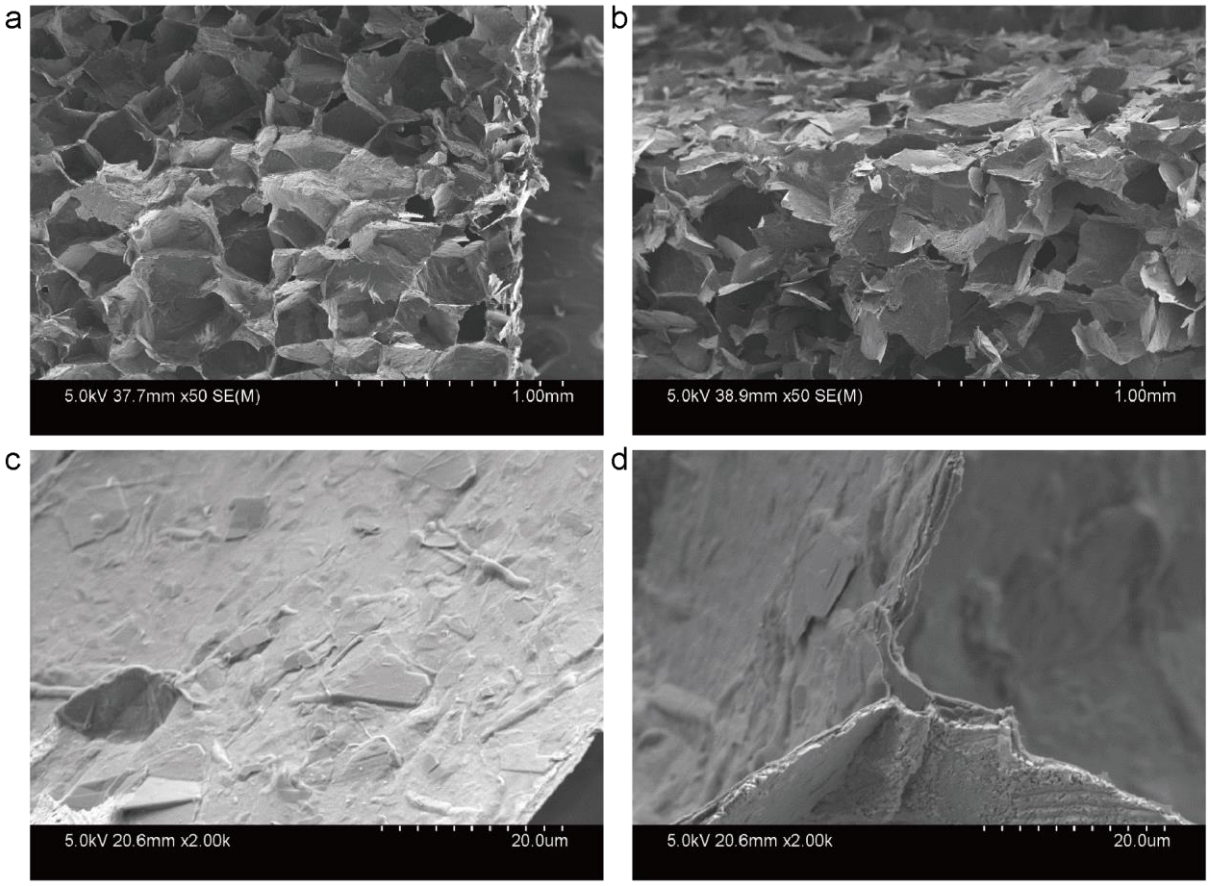

Figure S2. a,b, SEM image of the microstructure of the Cu-G-CNF foam. **c,d,** High-magnification SEM image of the Cu-G-CNF foam.

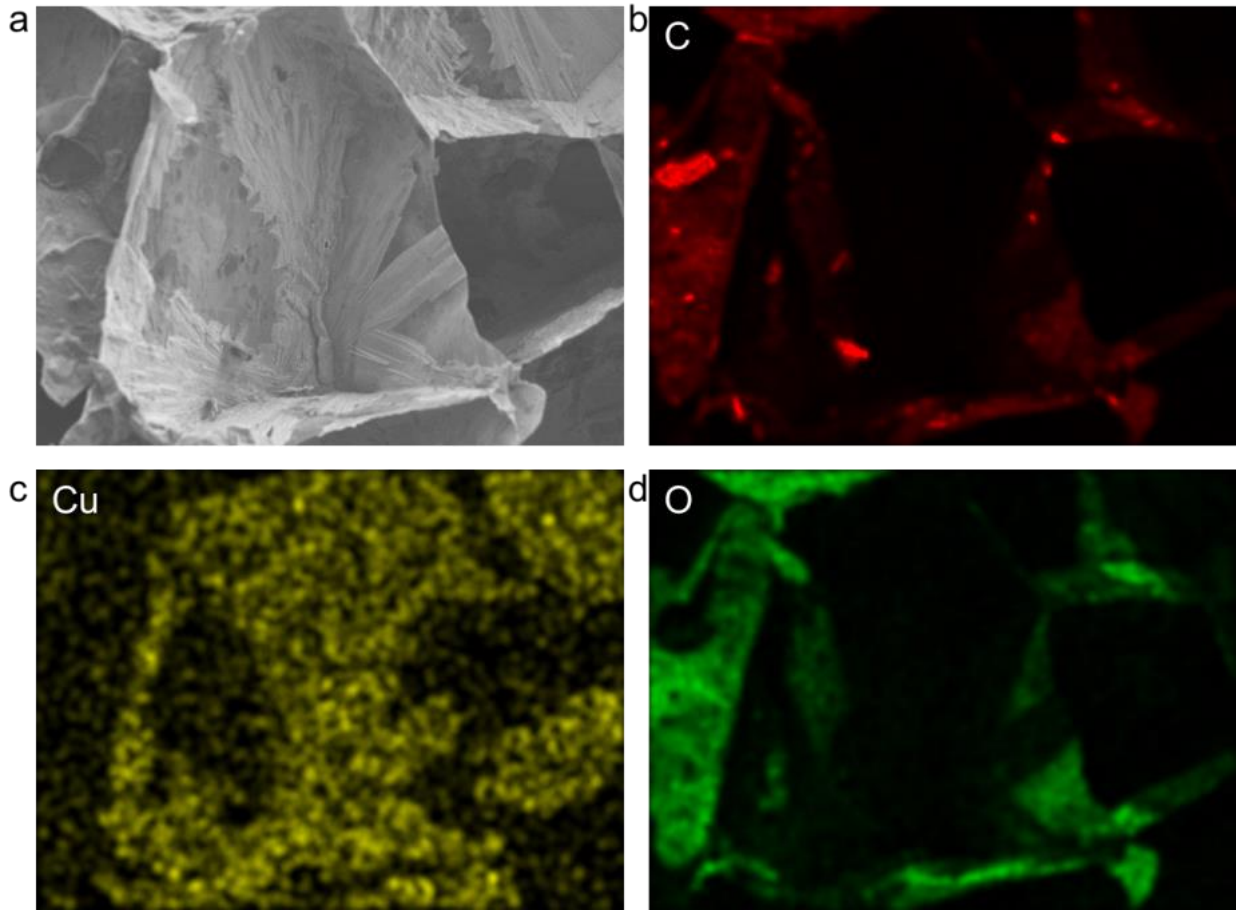

Figure S3. a, SEM image of the microstructure of the Cu-G-CNF foam. **b-d,** EDX mapping for the three detected elements: C, Cu, and O, respectively.

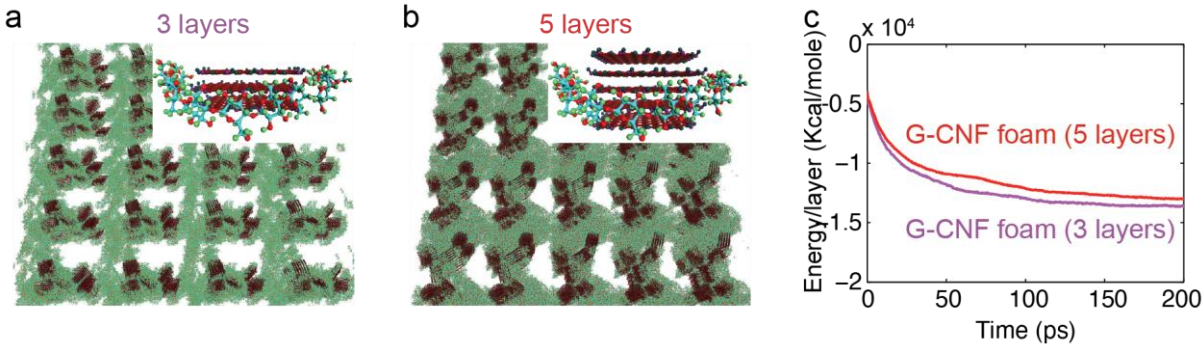

Figure S4. Atomistic structures of G-CNF foams with different number of graphene layers. **a,** G-CNF foam constructed with 3 layers of graphene. Insert shows the atomistic structure of three

graphene layers interacting with cellulose. **b,** G-CNF foam constructed with 5 layers of graphene. Insert shows the atomistic structure of five graphene layers interacting with cellulose. Brown and Green atoms represent the graphite flakes and cellulose chains, respectively. **c,** Variation of normalized hydrogen bonding energy as the function of time in the formation process of foam with three and five graphene layers.

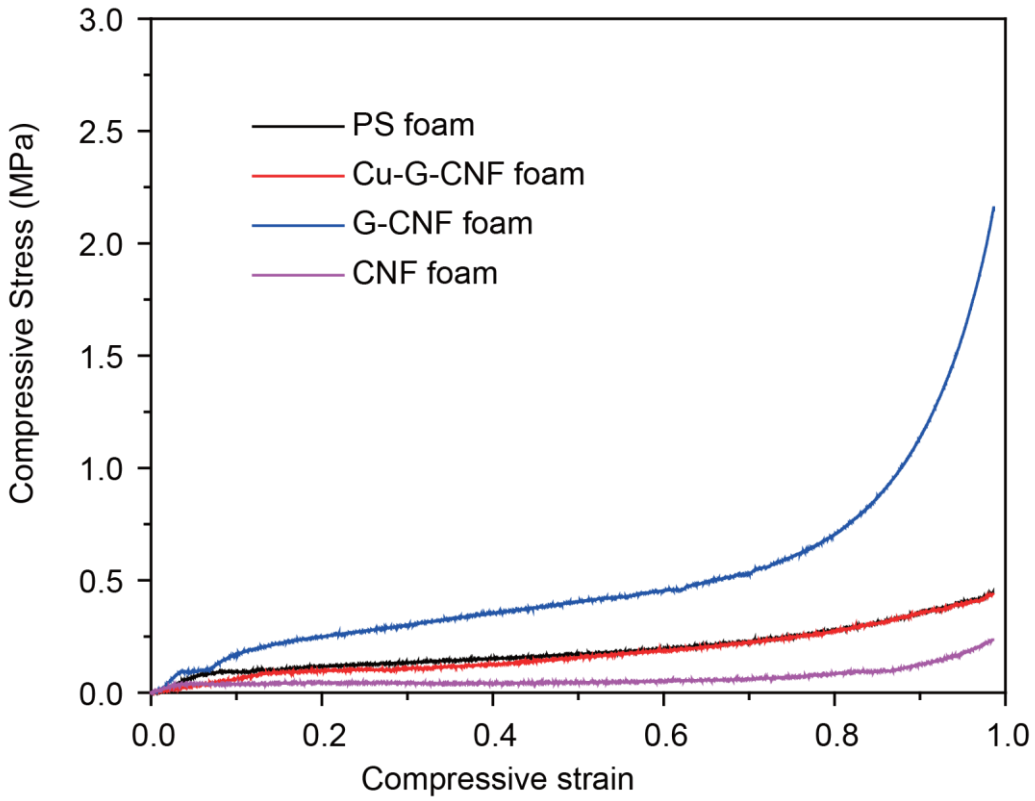

Figure S5. The compressive stress-strain curves of PS foam, CNF foam, graphite-CNF foam, and Cu^{2+} crosslinked G-CNF foam. The G-CNF foam showed a higher compressive strength of 2.2 MPa than other foams, and the crosslinked G-CNF foam showed a comparable compressive strength with the plastic PS foam.

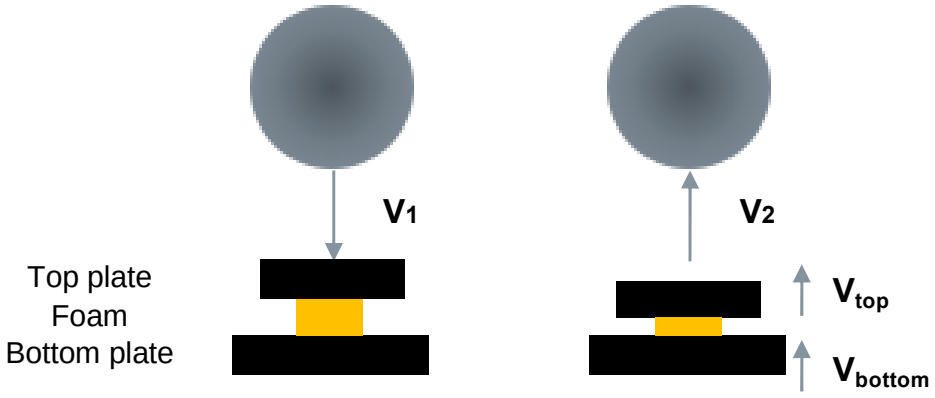

Figure S6. Configuration of the drop tower test. In the test, the drop weight was crashing towards the plates with an initial velocity V_1 given by gravity. After the crash, all the four components started to go upward with velocity of V_2, V_{top}, and V_{bottom}, respectively.

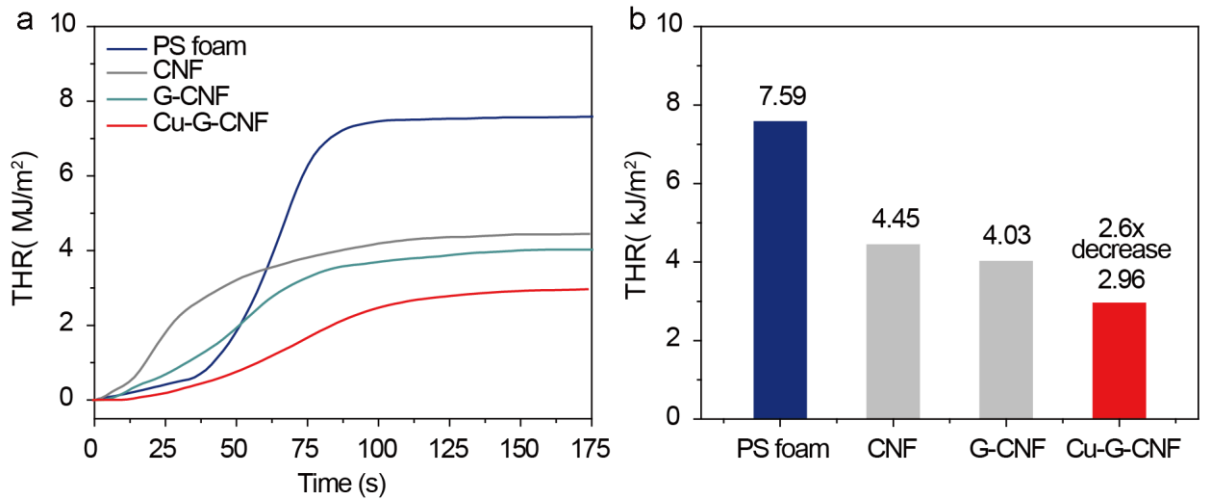

Figure S7. a, THR versus time. **b,** THR values of PS, CNF, G-CNF, and Cu-G-CNF foams. the reduction in THR for Cu-G-CNF foam is up to 61.0% compared with that of PS foam (2.96 MJ/m^2 vs.7.59 MJ/m^2). The significantly reduced THR of the Cu-G-CNF foam indicated the lower heat generated from the combustion of flammable volatiles escaped from the foam samples.

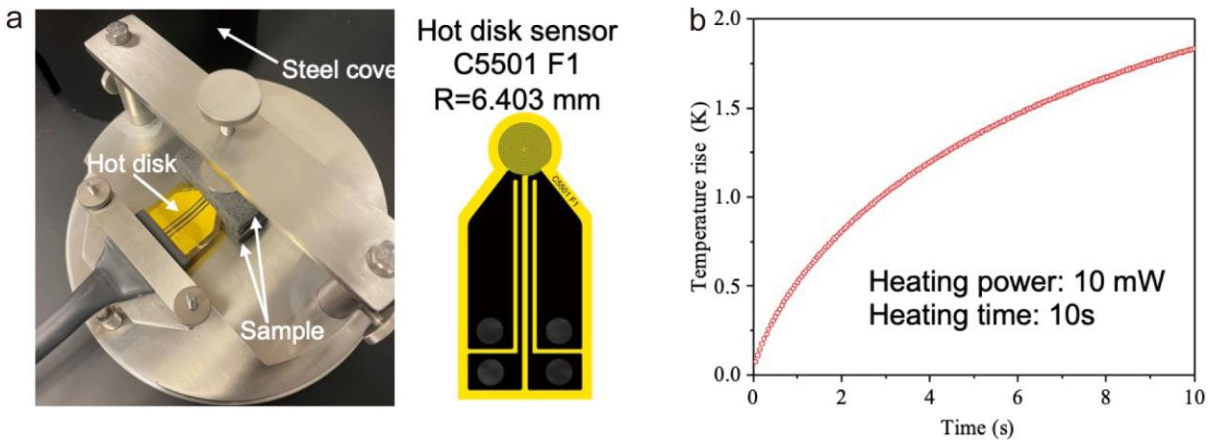

Figure S8. Thermal conductivity measurements. a, Thermal conductivity measurement setup. **b,** Time-temperature curve of the Cu-G-CNF foam sample during thermal conductivity measurement.

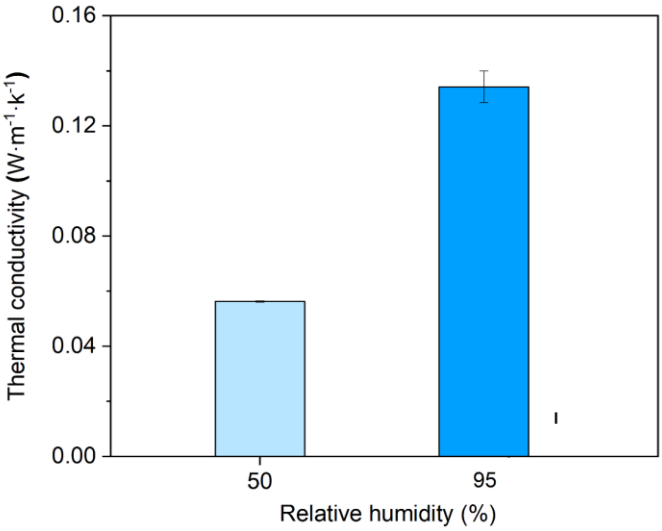

Figure S9. Thermal conductivities of Cu-G-CNF foam under 50% and 95% relative humidity conditions. The humidity-induced changes in the thermal conductivity were observed in the Cu-G-CNF foam. Under high humidity conditions (95% relative humidity), the water molecules condensed on the surface of the sample and reduce the thermal resistance, since the thermal conductivity of the water is significantly higher than that of the dry air. The thermal conductivities of the Cu-G-CNF foam increased from 0.056 to 0.134 W m^{-1} k^{-1} as relative humidity changed from 50% and 95%, indicating that the thermal conductivity of the Cu-G-CNF foam was significantly affected by relative humidity.

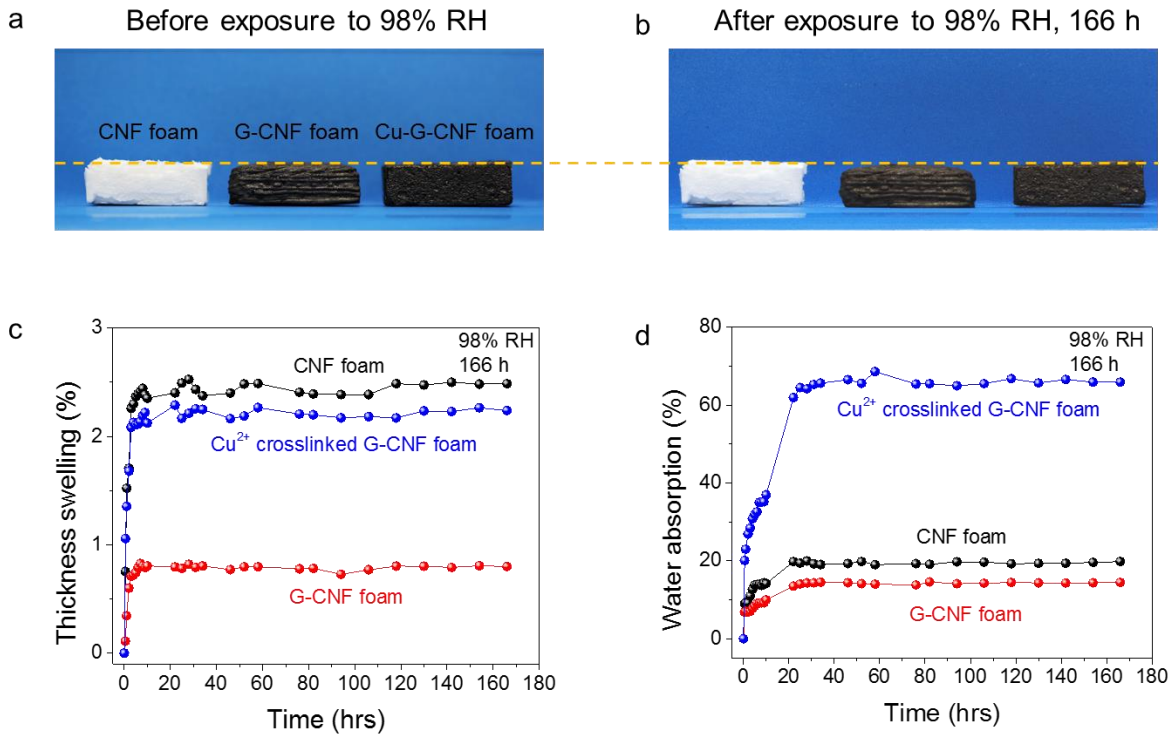

Figure S10. **a,b,** Photographs of the CNF foam, G-CNF foam and Cu^{2+} crosslinked G-CNF foam before (**a**) and after (**b**) sustaining 98% RH for 166 h. **c,d,** Change in thickness (**c**) and mass (**d**) of the three foams over time at 98% RH.

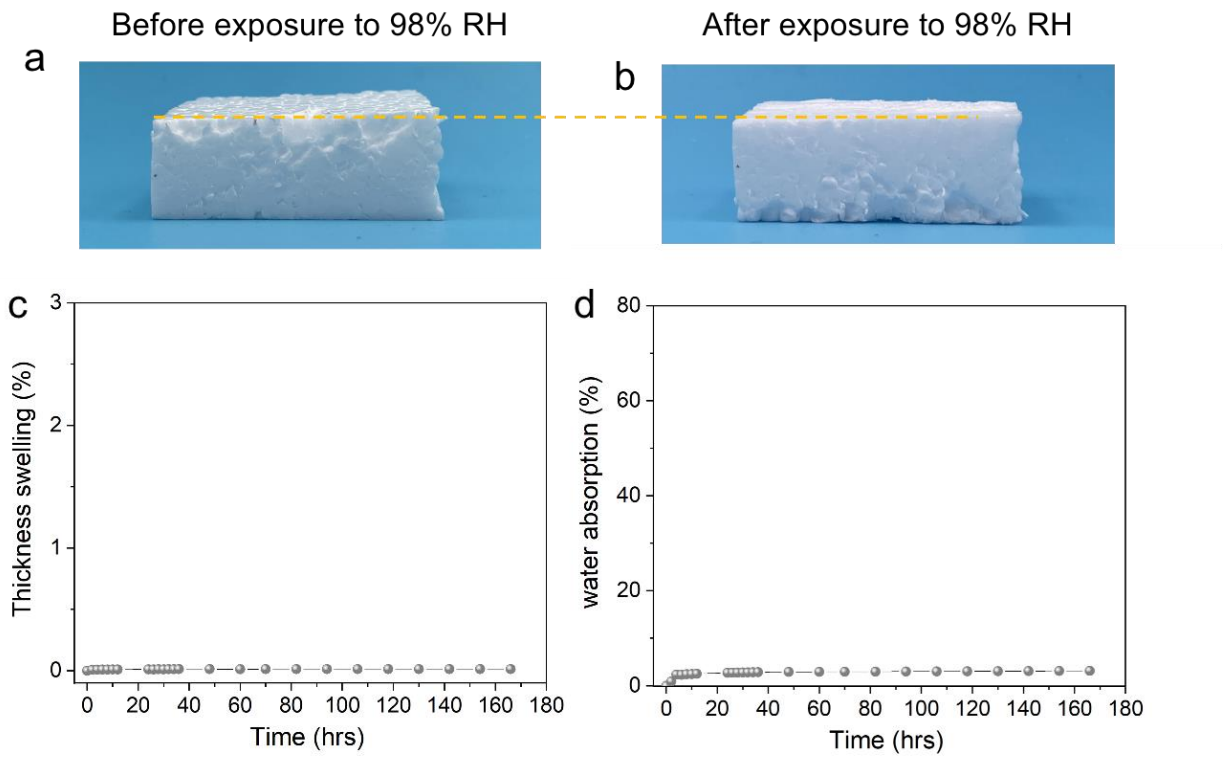

Figure S11. Photographs of the PS foam before (**a**) and after (**b**) sustaining 98% RH for 166 h. **c,d,** Change in thickness (**c**) and mass (**d**) of the PS foam over time at 98% RH. When exposed to high humidity condition, PS foam displayed basically no significant change, indicating good water stability of the PS foam.

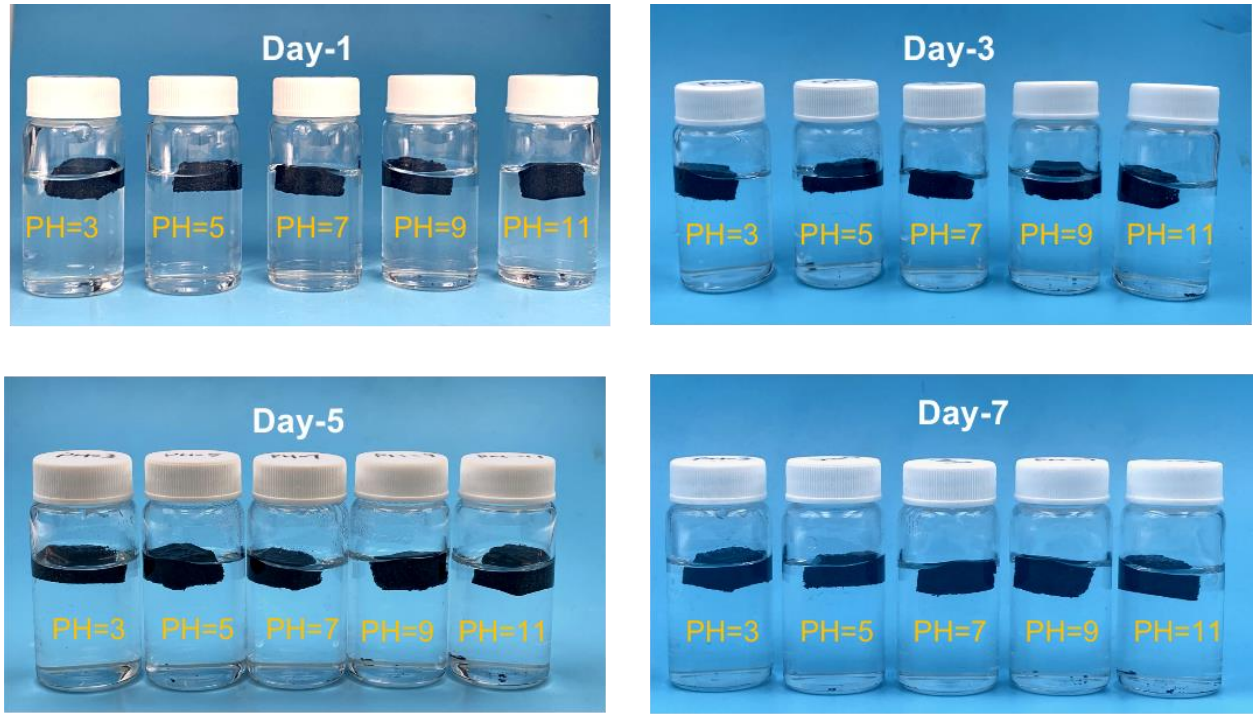

Figure S12. Optical pictures of Cu-G-CNF foam in variation of pH values solution for one week. No structure collapse of the foam material and color change in the solution during the 7-days continuous immersion in both the acid and alkaline solution, demonstrating good stability of the Cu-G-CNF foam even under acid and alkaline conditions without external stirring.

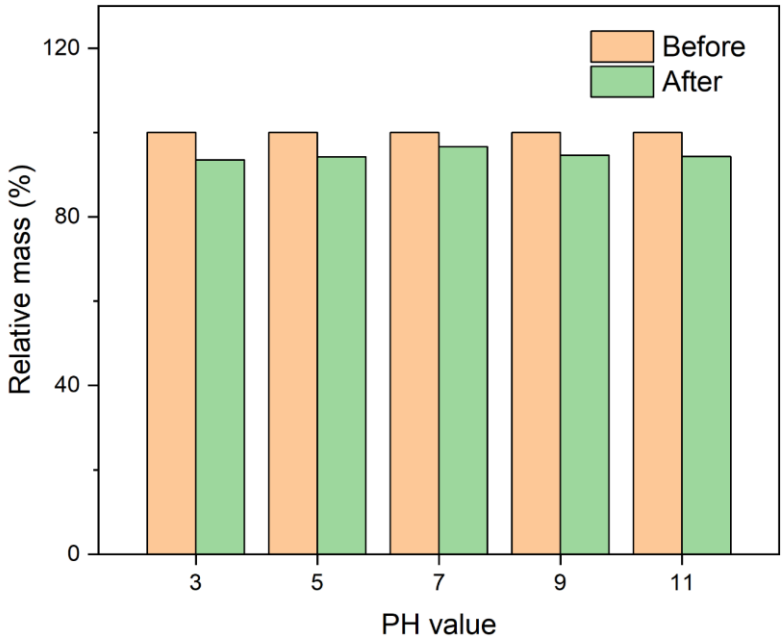

Figure S13. Relative mass of Cu-G-CNF foam before and after soaked in variation of pH values solution for one week. The mass of the Cu-G-CNF foam is slightly decrease after 7 days of immersion in the under acid and alkaline solution, demonstrating the outstanding stability of the prepared Cu-G-CNF foam with ionic crosslinking.

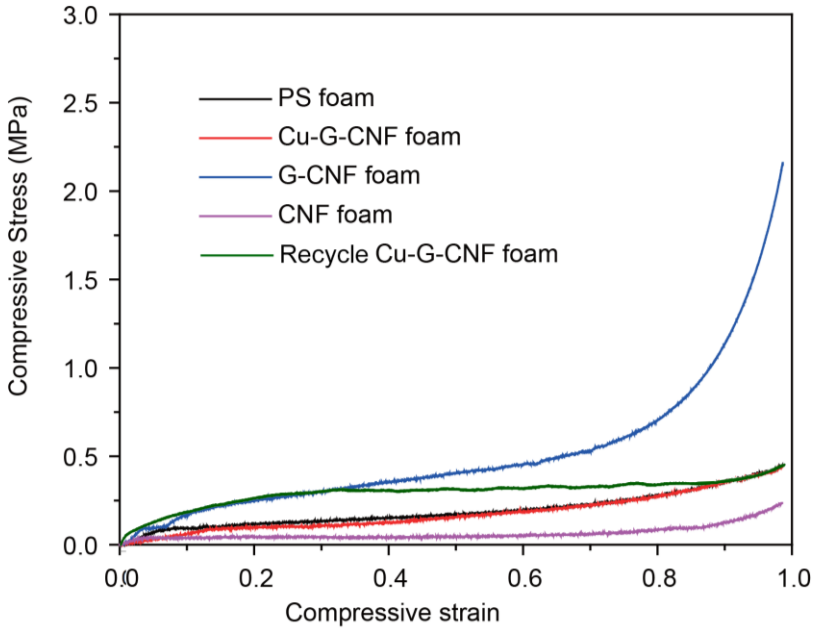

Figure S14. The compressive stress-strain curves of PS foam, CNF foam, graphite-CNF foam, Cu^{2+} crosslinked G-CNF foam, and recycle Cu^{2+} crosslinked G-CNF foam. The G-CNF foam showed a higher compressive strength of 2.2 MPa than other foams, and the crosslinked G-CNF foam showed a comparable compressive strength with the plastic PS foam.

Table S1. Drop tower tests results of 10 specimens.

Sample Name	Test #	Sample Thickness(mm)	V_1 (m/s)	V_2 (m/s)	V_{top}(m/s)	V_{bottom}(m/s)	$\Delta E_{kinetic}$ (J)
Aluminum 1	1	10	2.28	1.31	0.633	0.494	9.400
Aluminum 2	2	10	2.34	1.67	0.636	0.318	7.797
PS Foam 1	3	10	2.15	0.51	0.635	0.145	14.043
PS Foam 2	4	10	2.2	0.66	0.694	0.216	13.901
CNF Foam 1	5	10	2.3	0.23	0.154	0.265	17.052
CNF Foam 2	6	10	2.32	0.37	0.226	0.239	17.147
G-CNF Foam 1	7	10	2.41	0.31	0.407	0.327	18.209
G-CNF Foam 2	8	10	2.36	0.22	0.217	0.282	17.910
Cu-G-CNF Foam 1	9	10	2.39	0.23	0.466	0.292	18.135
Cu-G-CNF Foam 2	10	10	2.4	0.3	0.221	0.059	18.980

Table S2. Thermal properties of cellulosic foams/aerogels.

Raw materials	Thermal conductivity W/(mK)	Ref.
Cellulose nanofibril-alginate foam	0.03	6
Lignocellulosic nanofibrils aerogel	0.03	7
Konjac glucomannan/starch based aerogel	0.05	8
Carboxymethyl cellulose (CMC)/cellulose nanofibril (CNF) aerogel	0.05	9
Thin extruded fibers microcrystalline cellulosic aerogel	0.08	10
Aerogel-like carbon	0.08	11
Elium acrylic resin/cellulose nanofiber based composite aerogels	0.10	12
Natural wood based aerogel	0.12	13
Cu-G-CNF foam	0.05	This work

The Cu-G-CNF foam exhibits a low thermal conductivity of 0.05 W/(mK), as shown in Table S2, its heat-blocking ability is in the high class among the cellulose-based porous materials, suggesting that the Cu-G-CNF foam is a promising thermal insulation material.

Table S3. Average weight loss percentage of aerogel samples after 12 weeks of fungi degradation tests.

	Postia placenta	**Phanerochaete chrysosporium**	**Mixed mold fungi**
CNF	14.5% (5.40%)	6.23% (3.48%)	3.65% (1.53%)
G-CNF	9.54% (4.96%)	3.51% (1.80%)	2.64% (1.71%)
Cu-G-CNF	29.7% (7.79%)	19.80% (7.36%)	15.41% (5.61%)
PS	1.20% (2.33%)	0.89% (1.72%)	0.43% (0.70%)

*The percentage in bracket indicates the standard deviation of weight loss.

Supplementary References*:*

1. T. R. Mattsson, J. M. D. Lane, K. R. Cochrane, M. P. Desjarlais, A. P. Thompson, F. Pierce, G. S. Grest, First-principles and classical molecular dynamics simulation of shocked polymers. *Phys. Rev. B* **2010**, *81*, 054103.

2. S. Plimpton, Fast parallel algorithms for short-range molecular dynamics. *J. Comput. Phys.* **1995**, *117*, 1.

3. H. Zhu, S. Zhu, Z. Jia, S. Parvinian, Y. Li, O. Vaaland, L. Hu, T. Li, Anomalous scaling law of strength and toughness of cellulose nanopaper. *Proc. Natl. Acad. Sci.* **2015**, *112*, 8971.

4. American Society for Testing and Material, Standard test method for fungicides for controlling sapstain and mold on unseasoned lumber (laboratory method), in *ASTM Standard D4445-91*, West Conshohocken, PA, **1998**, vol. 11.01, pp. 497–500.

5. American Wood Protection Association, in *Book of Standards*, Birmingham, AL, **2013**, pp. 656

6. S. Jiang, M. Zhang, M. Li, J. Zhu, A. Ge, L. Liu, J. Yu, Cellulose-based composite thermal-insulating foams toward eco-friendly, flexible and flame-retardant. *Carbohydr. Polym*. **2021**, *273*, 118544.

7. Y. Zhu, Z. Yu, J. Zhu, Y. Zhang, X. Ren, F. Jiang, Developing flame-retardant lignocellulosic nanofibrils through reactive deep eutectic solvent treatment for thermal insulation. *Chem. Eng. J.* **2022**, *445*, 136748.

8. Y. Wang, K. Wu, M. Xiao, S. B. Riffat, Y. Su, F. Jiang, Thermal conductivity, structure and mechanical properties of konjac glucomannan/starch based aerogel strengthened by wheat straw. *Carbohydr. Polym.* **2018**, *197*, 284.

9. B. Chen, Q. Zheng, J. Zhu, J. Li, Z. Cai, L. Chen, S. Gong, Mechanically strong fully biobased anisotropic cellulose aerogels. *RSC Adv.* **2016**, *6*, 96518.

10. I. Karadagli, B. Schulz, M. Schestakow, B. Milow, T. Gries, L. Ratke, Production of porous cellulose aerogel fibers by an extrusion process. *J. Supercrit. Fluids* **2015**, *106*, 105.

11. Y.-Q. Li, Y. A. Samad, K. Polychronopoulou, K. Liao, Lightweight and Highly Conductive Aerogel-like Carbon from Sugarcane with Superior Mechanical and EMI Shielding Properties. *ACS Sustainable Chem. Eng.* **2015**, *3*, 1419.

12. R. Muthuraj, Y. Grohens, B. Seantier, Mechanical and thermal insulation properties of elium acrylic resin/cellulose nanofiber based composite aerogels. *Nano-Struct. Nano-Objects* **2017**, *12*, 68.

13. W. Guo, X. Wang, P. Zhang, J. Liu, L. Song, Y. Hu, Nano-fibrillated cellulose-hydroxyapatite based composite foams with excellent fire resistance. *Carbohydr. Polym.* **2018**, *195*, 71.